CrossMark

# On the Evolution of the Anisotropic Scaling of Magnetohydrodynamic Turbulence in the Inner Heliosphere

Nikos Sioulas[1] , Marco Velli[1,2] , Zesen Huang (黄泽森)[1] , Chen Shi (时辰)[1] , Trevor A. Bowen[3] , B. D. G. Chandran[4] ,
Ioannis Liodis[5] , Nooshin Davis[6] , Stuart D. Bale[3,7] , T. S. Horbury[8] , Thierry Dudok de Wit[9] , Davin Larson[3] ,
Michael L. Stevens[10] , Justin Kasper[11,12] , Christopher J. Owen[13] , Anthony Case[14] , Marc Pulupa[3] ,
David M. Malaspina[15,16] , Roberto Livi[3] , Keith Goetz[17] , Peter R. Harvey[3] , Robert J. MacDowall[18] , and John W. Bonnell[3]
[1] Department of Earth, Planetary, and Space Sciences, University of California, Los Angeles, Los Angeles, CA 90095, USA; nsioulas@ucla.edu
[2] International Space Science Institute, 3012 Bern, Switzerland
[3] Space Sciences Laboratory, University of California, Berkeley, CA 94720-7450, USA
[4] Space Science Center, University of New Hampshire, Durham, NH 03824, USA
[5] Department of Physics, Aristotle University of Thessaloniki, GR-52124 Thessaloniki, Greece
[6] Space Science Center and Department of Physics, University of New Hampshire, Durham, NH 03824, USA
[7] Physics Department, University of California, Berkeley, CA 94720-7300, USA
[8] The Blackett Laboratory, Imperial College London, London, UK
[9] LPC2E, CNRS and University of Orléans, Orléans, France
[10] Harvard-Smithsonian Center for Astrophysics, Cambridge, MA 02138, USA
[11] BWX Technologies, Inc., Washington, DC 20002, USA
[12] Climate and Space Sciences and Engineering, University of Michigan, Ann Arbor, MI 48109, USA
[13] Mullard Space Science Laboratory, University College London, Dorking, RH5 6NT, UK
[14] Smithsonian Astrophysical Observatory, Cambridge, MA 02138, US
[15] Astrophysical and Planetary Sciences Department, University of Colorado, Boulder, CO 80305, USA
[16] Laboratory for Atmospheric and Space Physics, University of Colorado, Boulder, CO 80303, USA
[17] School of Physics and Astronomy, University of Minnesota, Minneapolis, MN 55455, USA
[18] Solar System Exploration Division, NASA/Goddard Space Flight Center, Greenbelt, MD 20771, USA

## Abstract

We analyze a merged Parker Solar Probe (PSP) and Solar Orbiter (SO) data set covering heliocentric distances $13\,R_\odot \lesssim R \lesssim 220\,R_\odot$ to investigate the radial evolution of power and spectral index anisotropy in the wavevector space of solar wind turbulence. Our results show that anisotropic signatures of turbulence display a distinct radial evolution when fast, $V_{\rm sw} \geqslant 400\ {\rm km\ s}^{-1}$, and slow, $V_{\rm sw} \leqslant 400\ {\rm km\ s}^{-1}$, wind streams are considered. The anisotropic properties of slow wind in Earth orbit are consistent with a "critically balanced" cascade, but both spectral index anisotropy and power anisotropy diminish with decreasing heliographic distance. Fast streams are observed to roughly retain their near-Sun anisotropic properties, with the observed spectral index and power anisotropies being more consistent with a "dynamically aligned" type of cascade, though the lack of extended fast wind intervals makes it difficult to accurately measure the anisotropic scaling. A high-resolution analysis during the first perihelion of PSP confirms the presence of two subranges within the inertial range, which may be associated with the transition from weak to strong turbulence. The transition occurs at $\kappa d_i \approx 6 \times 10^{-2}$ and signifies a shift from $-5/3$ to $-2$ and from $-3/2$ to $-1.57$ scaling in parallel and perpendicular spectra, respectively. Our results provide strong observational constraints for anisotropic theories of MHD turbulence in the solar wind.

*Unified Astronomy Thesaurus concepts:* Interplanetary turbulence (830); Solar wind (1534); Space plasmas (1544); Magnetohydrodynamics (1964); Plasma astrophysics (1261)

## 1. Introduction

Magnetohydrodynamic (MHD) turbulence is relevant to a wide range of astrophysical systems such as stellar coronae, stellar winds, and the interstellar medium. A large-scale magnetic field $\boldsymbol{B}_0$[19] is often present (Parker 1979; Biskamp 2003), and the fluctuations are typically observed to be mostly incompressible. The incompressible MHD equations are better expressed using Elsässer variables, $\boldsymbol{z}^\pm = \boldsymbol{v} \pm \boldsymbol{b}$ (Elsässer 1950), where the nonlinear term for each variable may be written $\partial_t \boldsymbol{z}^\pm \sim -\boldsymbol{z}^\mp \cdot \nabla \boldsymbol{z}^\pm$ (here "$\sim$" means proportional up to a

projection operator ensuring incompressibility): nonlinear effects therefore require interactions between fluctuations with opposite signs of cross-helicity. Based on the weak interaction of oppositely moving Alfvénic wavepackets in a strong background magnetic field, $\delta v,\ \delta b \ll B_0$, i.e., assuming that the wave propagation $\tau_A(\boldsymbol{\kappa}) = 1/|\boldsymbol{B} \cdot \boldsymbol{k}|$ is shorter than the nonlinear decay time $\tau_{nl}(\boldsymbol{\kappa}) \approx 1/(k \cdot \delta u_k)$, where $\delta u_k$ is the average velocity fluctuation at scales $\ell \sim 1/|\boldsymbol{k}|$, the turbulent cascade will be slowed relative to hydrodynamic turbulence (Iroshnikov 1963; Kraichnan 1965). Assuming homogeneity, isotropy, $\boldsymbol{B} \cdot \boldsymbol{k} \to B \cdot k$, and scale locality of the interactions, simple dimensional analysis then leads to the prediction of the inertial range omnidirectional power spectrum, $E(k) \propto k^{-3/2}$. Magnetic fields, however, cannot be eliminated via Galilean transformations of MHD equations, as opposed to mean velocity fields, $\boldsymbol{V}_0$, resulting in strongly anisotropic turbulent dynamics (Montgomery & Turner 1981; see also reviews by Schekochihin et al. 2009; Oughton et al. 2015, and references

---

[19] Magnetic fields are presented in Alfvén velocity units, e.g., $\boldsymbol{b} \to \boldsymbol{b}/\sqrt{4\pi\rho}$, $\boldsymbol{B}_0 \equiv \boldsymbol{V}_a$.

therein). In particular, conservation of energy and momentum during wave−wave interactions (more specifically, a wave−2D perturbation interaction; see Montgomery & Matthaeus 1995) allows power to cascade down to smaller scales perpendicular to $\boldsymbol{B}_0$, resulting in a two-dimensionalization of the turbulence spectrum in a plane transverse to the locally dominant magnetic field, while at the same time inhibiting spectral energy transfer along the direction parallel to the field (Shebalin et al. 1983; Ng & Bhattacharjee 1996; Galtier et al. 2000).

A multitude of observational and numerical studies have investigated the manifestations of anisotropy in the presence of an energetically significant mean magnetic field, e.g., anisotropy in correlation functions, power at a fixed scale, spectral indices, intermittency (Belcher & Davis 1971; Matthaeus et al. 1990; Bieber et al. 1996; Maron & Goldreich 2001; Weygand et al. 2009; Beresnyak & Lazarian 2010; Osman et al. 2012; Wicks et al. 2013; Chandran & Perez 2019; Pine et al. 2020; Bandyopadhyay & McComas 2021; Zank et al. 2022; Sioulas et al. 2022b; Chhiber 2022; Dong et al. 2022). A comprehensive overview of the various forms of anisotropy can be found in Horbury et al. (2012).

Using in situ observations in the solar wind, Horbury et al. (2008), Podesta (2009), and Chen et al. (2010) explored the dependence of the scaling index of the magnetic power spectrum's inertial range, $\alpha_B$, on the field/flow angle $\theta_{BV}$. An essential nuance in observing scale-dependent anisotropy involves the necessity of measuring parallel correlations along a local, scale-dependent mean magnetic field, $\boldsymbol{B}_\ell$, instead of the global mean magnetic field, as emphasized by Cho & Vishniac (2000) and Gerick et al. (2017) (see also review by Schekochihin 2022, and references therein). The aforementioned studies suggest inertial range spectral indices of $-2$ and $-5/3$ for flow directions parallel ($\Theta_{BV} \approx 0°$) and perpendicular ($\Theta_{BV} \approx 90°$) to the mean magnetic field, respectively. These observations were interpreted as supporting evidence for the critical balance (CB) theory (Sridhar & Goldreich 1994; Goldreich & Sridhar 1995, 1997),[20] which is based on the conjecture that the inertial range dynamics of MHD turbulence with vanishing cross-helicity ($\sigma_c \approx 0$), later extended to imbalanced cascades (Lithwick et al. 2007), are governed by wavevector modes for which rough equality between $\tau_A(\boldsymbol{\kappa})$ and $\tau_{nl}(\boldsymbol{\kappa})$, $\tau_A(\boldsymbol{k}) \approx \tau_{nl}(|\boldsymbol{k}|)$, holds. As a result, the relationship between the parallel and perpendicular wavevectors follows an anisotropic scaling, $\kappa_\parallel \sim \kappa_\perp^{2/3}$. Based on this scaling, we expect the magnetic fluctuation spectra to follow scalings of $E(k_\perp) \propto k_\perp^{-5/3}$ and $E(k_\parallel) \propto k_\parallel^{-2}$. However, the dynamic alignment conjecture (Boldyrev 2006; Mason et al. 2006; Perez & Boldyrev 2009) suggests that, as the energy cascades to smaller scales, velocity and magnetic field fluctuations in the plane perpendicular to $\boldsymbol{B}_\ell$ will align to within a smaller angle $\phi$, resulting in weaker nonlinear interactions and a flatter perpendicular inertial range spectrum, $E(k_\perp) \propto k_\perp^{-3/2}$. In contrast, the field parallel spectrum remains unchanged, $E(k_\parallel) \propto k_\parallel^{-2}$. Other models of turbulence, such as the 2D plus slab model (Zank et al. 2020), lead to perpendicular and parallel spectra that can range between 5/3 and 3/2 in the perpendicular direction and between 5/3 and 2 in the parallel direction.

Recent observations from the Parker Solar Probe (PSP) and Solar Orbiter (SO) missions have provided the opportunity to investigate the radial evolution of turbulence in the inner

heliosphere. It was shown that the inertial range of the magnetic spectrum grows with distance, progressively extending to larger spatial scales (Sioulas et al. 2022a) while at the same time steepening from a scaling of $\alpha_B = -3/2$ at approximately 0.06 au toward the Kolmogorov scaling of $\alpha_B = -5/3$ (Chen et al. 2020; Alberti et al. 2020; Telloni et al. 2021; Shi et al. 2021; Zhao et al. 2022). The rate at which the spectrum steepens has also been found to be related to the Alfvénic content and magnetic energy excess of the fluctuations (Sioulas et al. 2022a). On the contrary, the spectral index of the velocity spectrum in the inertial range has consistently been found to be close to $\alpha_v = -3/2$, regardless of the distance from the Sun (Shi et al. 2021).

In this study, we aim to understand the radial evolution of anisotropic magnetic turbulence in the inner heliosphere. To do this, we analyze data from the PSP and SO missions covering heliocentric distances $13\,R_\odot \lesssim R \lesssim 220\,R_\odot$ using wavelet analysis. This technique allows us to decompose the magnetic field time series into scale-dependent background and fluctuations and study the dependence of the turbulence properties on the field/flow angle $\theta_{BV}$.

The rest of the paper is structured as follows: In Section 2, we provide background on wavelet analysis and introduce the anisotropy diagnostics used in this study. Section 3 presents the selection and processing of the data. The results of this study are presented in Section 4, with a focus on high-resolution data obtained during the first perihelion of PSP in Section 4.1 and the radial evolution of magnetic field anisotropy investigated in Section 4.2. In Section 6, we compare our findings to previous relevant studies in order to advance our understanding of the topic and validate our conclusions. The discussion of the results and conclusions are provided in Sections 5 and 7, respectively.

## 2. Diagnostics

### 2.1. Wavelet Analysis and Estimation of Power Spectral Density

Anisotropy in turbulence represents a local property that relies on both the position and scale. The turbulent fluctuations at a given scale $\ell$ are greatly influenced by the local mean magnetic field of a size that ranges between $3\ell$ and $5\ell$ (Gerick et al. 2017). To analyze anisotropy, wavelet analysis has proven to be a useful technique, as it allows signal decomposition into components that are localized in both time and wavelet scale. Recently, the continuous wavelet transform (CWT) has been extensively utilized to estimate the power of magnetic field fluctuations as a function of the direction of the local mean magnetic field (Podesta 2009; Wicks et al. 2010). For a discrete set of measurements such as the time series of the $i$th component of the magnetic field $B_i$, where $i = R,\ T,\ N$, and resolution $\delta t$, the wavelet transform is defined as

$$\omega_i(\ell,\ t_n) = \sum_{j=0}^{N-1} B_i(t_j)\psi^*\left(\frac{t_j - t_n}{\ell}\right), \qquad (1)$$

where $\psi^*$ denotes the conjugate of the Morlet mother wavelet and $\psi(t) = \pi^{-1/4}[e^{i\omega_0 t} - e^{-\frac{\omega_0^2}{2}}]e^{-\frac{t^2}{2}}$. The parameter $w_0$, representing the frequency of the wavelet, is set equal to $w_0 = 6$. The transformation from the dilation scale, $\ell$, to the physical spacecraft frequency, $f_{sc}$, is given by

$$f_{sc} = \frac{w_0}{2\pi\ell\Delta t}, \qquad (2)$$

---

[20] Heavily influenced by the work of Higdon (1984).

where $\Delta t$ represents the time interval between successive measurements. The power spectral density (PSD) of the $i$th component as a function of spacecraft frequency $f_{sc}$ and the local, scale-dependent field/flow angle $\theta_{BV}$ can be estimated as

$$F_{ii}(f_{sc}, \ \theta_{BV}) = \frac{2\delta t}{N} \sum_{n=0}^{N-1} |\omega_i(\ell, t_n, \theta_{BV})|^2, \quad (3)$$

Here $N$ is the number of samples within the range $\theta_{j-1} \leqslant \theta_{BV} \leqslant \theta_j$, $\theta_j = 5° \cdot j$, $j = 0, 1, ..., 18$. At time $t_n$ and wavelet scale $\ell$, we estimate the angle $\theta_{BV}$ using the scale-dependent local mean magnetic field $\boldsymbol{B}_\ell$ and velocity field $\boldsymbol{V}_\ell$, where $\boldsymbol{V}$ represents the solar wind velocity in the spacecraft frame (Duan et al. 2021; Cuesta et al. 2022). To calculate the scale-dependent local mean of a field, $\boldsymbol{q}$, we use a Gaussian weighting scheme centered at $t_n$:

$$\boldsymbol{q}_\ell(t_n, \ell) = \sum_{m=0}^{N-1} \boldsymbol{q}_m \exp\left(-\frac{(t_n - t_m)^2}{2\lambda^2\ell^2}\right), \quad (4)$$

where $\lambda$ is a dimensionless parameter that determines the scaling of the average. To ensure the robustness of our findings, we investigated two distinct values of $\lambda$, specifically $\lambda = 1$ and $\lambda = 3$. Remarkably, the results obtained for both cases were comparable, exhibiting differences in spectral exponents of only $0.01-0.02$ (see also Gerick et al. 2017). The parameter $\theta_{BV}$ was determined using two distinct methods: the non-scale-dependent time-to-time velocity field value $\boldsymbol{V}(t)$ and the scale-dependent value $\boldsymbol{V}_\ell$. Our results indicates that the outcomes obtained from both techniques are practically indistinguishable, which validates the minimal impact of interpolating $\boldsymbol{V}$ at the time points of $\boldsymbol{B}$ or only considering $\boldsymbol{V}(t)$ (see also Verdini et al. 2018; Wang et al. 2020). Throughout the remainder of the study, we utilize $\boldsymbol{B}_\ell$ and $\boldsymbol{V}_\ell$ to estimate the $\theta_{BV}$ parameter considering the case where $\lambda = 3$. For intervals that are sampled at heliocentric distances greater than 0.5 au and have a significant lack of plasma data, defined as having more than 10% of solar wind velocity measurements missing, the angle $\theta_{BR}$ is used. This angle represents the angle between $\boldsymbol{B}_\ell$ and the scale-dependent radial component of the magnetic field, denoted as $B_{R\ell}$. To determine the reliability and consistency of using $\theta_{BR}$ instead of $\theta_{BV}$, both angles were evaluated for intervals with adequate plasma data. Our findings suggest that the anisotropic spectra remained almost unchanged for the majority of intervals, even when sampled as close as 0.3 au. The subsequent analysis examines the trace of the PSD, denoted as $F = \sum F_{ii}$. The range of $\theta_{BV}$ is restricted to be between 0° and 90° based on the symmetry of $\theta_{BV}$ around 90° (Chen et al. 2011).

To transform the PSD derived in the spacecraft-frame frequency $F(f_{sc}, \ \theta_{BV})$ into a wavenumber spectrum expressed in physical units $E(\kappa^*, \ \theta_{BV})$, we employ Taylor's frozen-in hypothesis (Taylor 1938). This hypothesis assumes that the speeds of MHD wave modes, such as shear Alfvén modes propagating at $V_p = V_A \cos(\langle \boldsymbol{k}, \boldsymbol{B} \rangle)$ observed in the solar wind plasma, are negligible compared to the bulk flow of the solar wind. This means that the Alfvén Mach number $M_A = \frac{V_r}{V_A} \gg 1$. However, as the PSP spacecraft approaches the Sun, both the spacecraft velocity $\boldsymbol{V}_{sc}$ and the speeds of MHD wave modes start to become comparable to $\boldsymbol{V}_{sw}$ (Perez et al. 2021). For this reason, a modified version of Taylor's hypothesis that accounts

for wave propagation and spacecraft velocity is adopted for heliocentric distances below 0.3 au, i.e., $\kappa^* = \kappa \cdot d_i = 2\pi f_{sc}/V_{tot} \cdot d_i$, where $d_i$ represents the ion inertial length and $V_{tot} = |\boldsymbol{V}_{sw} + Va - \boldsymbol{V}_{sc}|$ (Klein et al. 2015; Zank et al. 2022; Zhao et al. 2022). It is important to note that this method assumes the dominance of outwardly propagating waves, which is the case for the vast majority of the analyzed intervals closer to the Sun (Alberti et al. 2022; Sioulas et al. 2022a).

## 3. Data Selection and Processing

### 3.1. Data Selection

As a first step, observations of PSP between 2018 January 1 and 2022 October 1 were collected, encompassing the first 13 perihelia (E1−E13) of the PSP mission. Level 2 magnetic field data from the fluxgate magnetometer (FGM; Bale et al. 2016), as well as Level 3 plasma moment data from the Solar Probe Cup (SPC) for E1−E8 and the Solar Probe Analyzer (SPAN) from the Solar Wind Electron, Alpha and Proton (SWEAP) suite for E9−E13 (Kasper et al. 2016), were analyzed. Data from the SCaM product (Bowen et al. 2020) obtained during E1 have also been analyzed and will be presented as a high-quality case study. The plasma data consist of moments of the distribution function computed on board the spacecraft, including the proton velocity vector $\boldsymbol{V}_p$, number density $n_p$, and temperature $T_p$. When available, electron number density data derived from the quasi-thermal noise from the FIELDS instrument (Moncuquet et al. 2020) were preferred over SPAN or SPC data for estimating proton number density. In order to calculate the proton density from the electron density, charge neutrality must be considered, leading to a $\approx 4\%$ abundance of alpha particles. Therefore, electron density from quasi-thermal noise was divided by 1.08.

The second step involved obtaining magnetic field and particle measurements from the SO mission between 2018 June 1 and 2022 March 1. Magnetic field measurements from the Magnetometer (MAG) instrument (Horbury et al. 2020) have been analyzed using burst magnetic field data when available. Particle moment measurements for our study are provided by the Proton and Alpha Particle Sensor (SWA-PAS) on board the Solar Wind Analyser (SWA) suite of instruments (Owen et al. 2020).

### 3.2. Data Processing

Quality flags for the magnetic field and particle time series have been taken into account, and time intervals missing $\geqslant 1\%$ and/or $\geqslant 10\%$ in the magnetic field and particle time series have been omitted from further analysis. Additionally, the mean value of the cadence between successive measurements $\delta\tau$ in the magnetic field time series has been estimated for each of the selected intervals, and time intervals that were found to have a mean cadence of $\delta\tau \geqslant 250$ ms were discarded. Due to poor data quality, all PSP intervals exceeding $R \simeq 0.5$ au have also been discarded.

Spurious spikes in the plasma time series were eliminated by replacing outliers exceeding three standard deviations within a moving average window covering 200 points with their median values (Davies & Gather 1993).
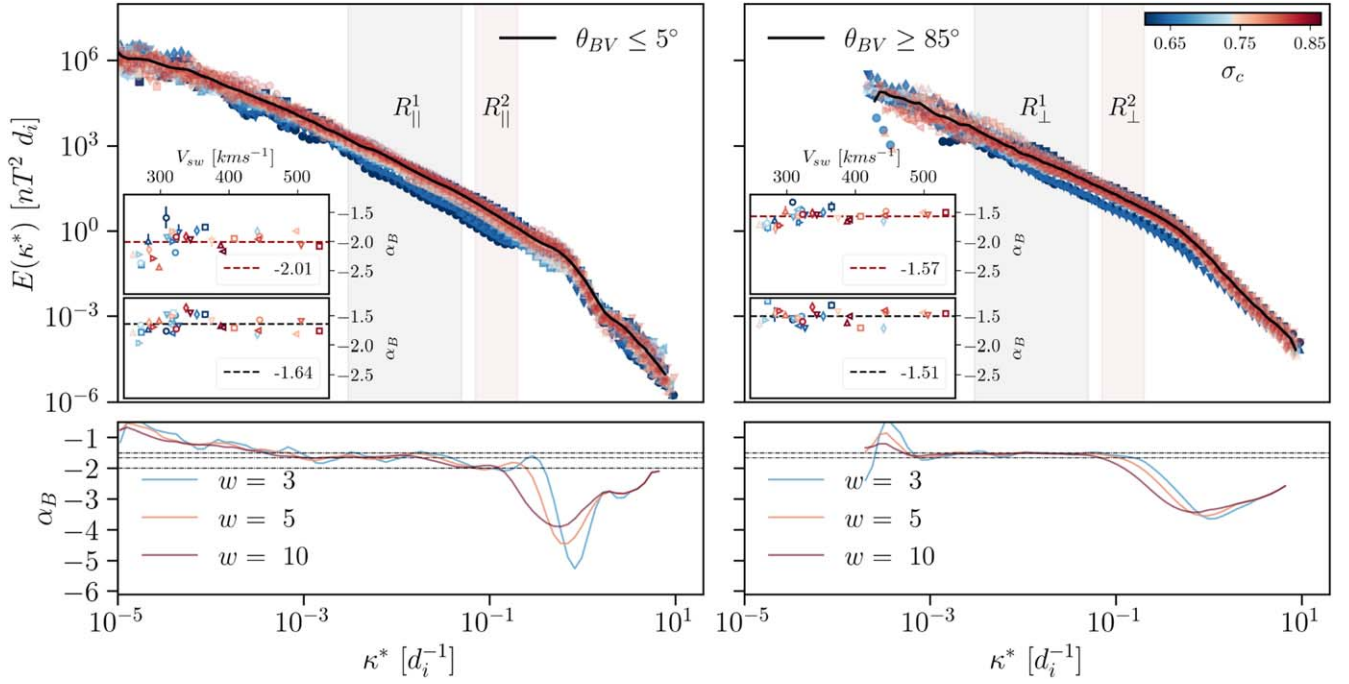
**Figure 1.** Averaged magnetic field power spectrum (black solid line) for fluctuations parallel ($\theta_{BV} \leqslant 5°$; left panel) and perpendicular ($\theta_{BV} \geqslant 85°$; right panel) to the local magnetic field during the first perihelion of PSP (E1) estimated using SCaM data. The dependence of the spectra on normalized cross-helicity ($\sigma_c$) is also shown, with the color keyed to $\sigma_c$. The inset figures illustrate the spectral index $\alpha_B$, at two different ranges of scales (bottom) $3 \times 10^{-3} d_i - 5 \times 10^{-2} d_i$ and (top) $8 \times 10^{-2} d_i - 2 \times 10^{-1} d_i$ as a function of solar wind speed and $\sigma_c$. The dashed horizontal lines indicate the mean value of $\alpha_B$. The second row illustrates the local $\alpha_B$, calculated over a sliding window of a factor of 3, 5, and 10 shown in cyan, orange, and red, respectively. Horizontal dotted lines have also been added marking values $-3/2$, $-5/3$, and $-2$.

## 4. Results

### 4.1. Case Study: SCaM Data Set, E1

The high-resolution data from the first perihelion of the PSP ($R \approx 0.17$ au) from 2018 November 1 to 11 were analyzed. A total of 33 intervals, each with a duration of 12 hr, were obtained, and the PSD was estimated, with subsequent intervals overlapping by 50%. The analysis covered 18 bins of the $\theta_{BV}$ angle, but in the following we will only focus on those bins closer to the parallel and perpendicular directions, with $\theta_{BV} \leqslant 5°$ and $\theta_{BV} \geqslant 85°$, respectively. It is worth noting that the second half of E1 displayed significantly different characteristics compared to the first half, with the solar wind exhibiting higher speeds and a greater number of magnetic switchbacks (Bale et al. 2019). It is well established that power spectra exhibit different characteristics when different solar wind speeds are considered owing to the different types of fluctuations they transport (Borovsky et al. 2019). Specifically, the fast solar wind is highly Alfvénic and characterized by large-amplitude, incompressible fluctuations, while the slow wind is generally populated by smaller-amplitude, less Alfvénic, compressive fluctuations, which include convected coherent structures (Bruno et al. 2003; Matteini et al. 2014; Shi et al. 2021; Sioulas et al. 2022b; Zhao et al. 2020). Consequently, the spectral variation due to the differing plasma parameters of the selected streams was investigated. More specifically, we considered the dependence of the PSD on the solar wind speed, $V_{sw}$, the normalized cross-helicity $\sigma_c$,

$$\sigma_c = \frac{E_o - E_i}{E_o + E_i}, \quad (5)$$

a measure of the relative amplitudes of inwardly and outwardly propagating Alfvén waves (AWs), and the normalized residual energy $\sigma_r$,

$$\sigma_r = \frac{E_V - E_b}{E_V + E_b}, \quad (6)$$

indicating the balance between kinetic and magnetic energy, where $E_\phi = \frac{1}{2} \langle \delta\phi^2 \rangle$ denotes the energy associated with the fluctuations of the field $\phi$. In particular, $E_{o,i}$ can be estimated using Elsässer variables, defining outward- and inward-propagating Alfvénic fluctuations (Velli et al. 1991; Velli 1993)

$$\delta \boldsymbol{Z}_{o,i} = \delta \boldsymbol{V} \mp sign(B_0^R) \delta \boldsymbol{b}, \quad (7)$$

where $\delta \boldsymbol{B} = \boldsymbol{B} - \boldsymbol{B}_0$, with $\boldsymbol{B}_0$ the background magnetic field, $\delta \boldsymbol{b} = \delta \boldsymbol{B} / \sqrt{\mu_0 m_p n_p}$ the magnetic fluctuations in Alfvén units, and $B_0^r$ the ensemble average of $B_R$, utilized to determine the polarity of the radial magnetic field (Shi et al. 2021). The magnetic field power spectra for fluctuations parallel ($\theta_{BV} \leqslant 5°$) and perpendicular ($\theta_{BV} \geqslant 85°$) to the local magnetic field, resulting from averaging all the respective spectra, are presented in Figure 1. Individual spectra are also shown with the color of the curve keyed to $\sigma_c$. The fluctuation power in the MHD range shows a positive correlation with $\sigma_c$, but this dependence vanishes in the transition region and kinetic scales. A similar trend was observed with $\sigma_r$ and $V_{sw}$, not shown here. The results are consistent with Vasquez et al. (2007), who found higher, MHD range, turbulence amplitudes associated with faster streams, as well as Pi et al. (2020), who showed that such dependence vanishes in the kinetic scales. The trend also vanishes at the large, energy injection scales, $\kappa d_i \leqslant 10^{-3}$, where
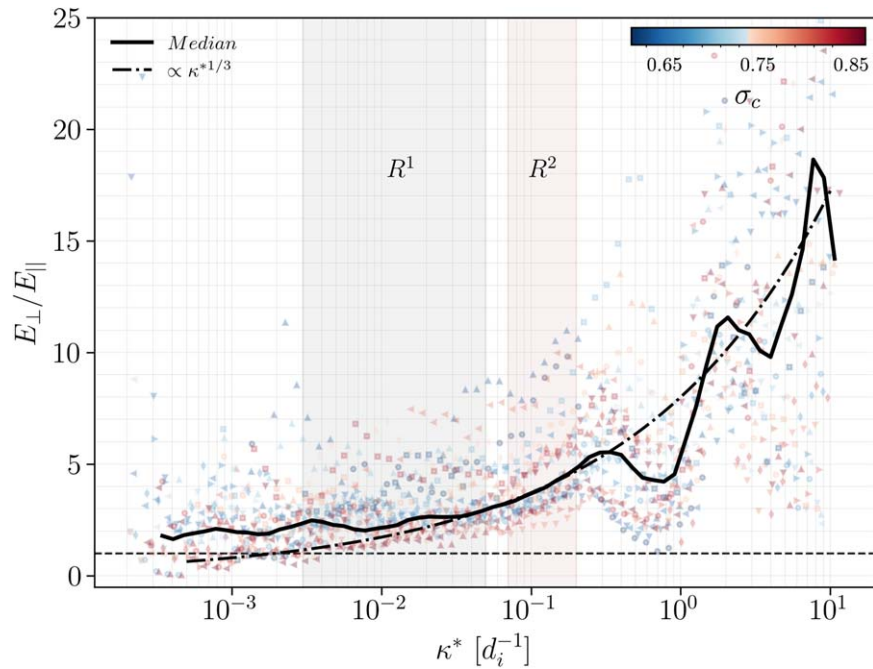
**Figure 2.** The anisotropy of the fluctuations described by the ratio of the perpendicular ($E_\perp$) to the parallel power ($E_\parallel$). A horizontal black dashed line has been added to indicate $E_\perp/E_\parallel = 1$.

the power spectrum is clearly dominated by parallel fluctuations. Focusing our attention on MHD scales, we can observe two distinct ranges, roughly $3 \times 10^{-3} \kappa d_i - 5 \times 10^{-2} \kappa d_i$ and $8 \times 10^{-2} \kappa d_i - 2 \times 10^{-1} \kappa d_i$, over which the PSD displays a clear power-law scaling. Light-black and red shadings are used to indicate these regions in the figure, and we will thereby refer to them as $R^1_{\parallel(\perp)}$ and $R^2_{\parallel(\perp)}$. The power-law fitting has been applied to the PSD for the two ranges, and the bottom and top inset figures illustrate $\alpha_B$ as a function of $V_{\rm sw}$. Note that the color of the scatter plot is keyed to $\sigma_c$. Furthermore, horizontal lines have been added to indicate the average value of $\alpha_B$. In the direction parallel to the mean field the PSD scales roughly like $-5/3$ and $-2$ in $R^1_\parallel$ and $R^2_\parallel$, respectively. For perpendicular fluctuations, only a minor difference may be observed between $R^1_\perp$ and $R^2_\perp$, which are characterized by a power-law scaling with index $-3/2$ and $-1.57$, respectively. The absence of a definitive correlation between $\alpha_B$, $V_{\rm sw}$, and $\sigma_c$, as reported in the study by Sioulas et al. (2022a), could be ascribed to the relatively extended time intervals that were examined or the limited size of the sample, which, in this case, encompassed only 33 intervals.

When examining the local spectral index, $\alpha_B(\kappa^*)$, a similar pattern emerges. This is achieved by applying a sliding window of size $w = 3, 5, 10$ in $\kappa^*$ over the spectra and calculating the best-fit linear gradient in log−log space over this window, shown in cyan, orange, and red, respectively, in the bottom panel of Figure 1. At smaller scales where $\kappa^* \geqslant 0.1 d_i^{-1}$, both parallel and perpendicular fluctuations display a steeper spectrum between the inertial and kinetic ranges. The scaling behavior observed in the transition and kinetic ranges is consistent with the findings reported by Duan et al. (2021). Additionally, Duan et al. (2021) report a scaling exponent of $-2$ for the parallel spectrum in the inertial range spanning from $4 \times 10^{-1}$ Hz to 2 Hz, which corresponds to region $R^2_\parallel$ in our analysis. It is worth noting, however, that $R^2_\parallel$ does not

encompass the entire inertial range. Specifically, $R^1_\parallel$ covers most of the MHD range and is characterized by a shallower scaling exponent, $\alpha_B \approx -5/3$. The two different MHD scalings persist in most of the intervals studied, suggesting that this may be a consistent feature of the solar wind power spectrum in the vicinity of the Sun.

We then analyzed the power anisotropy, defined as $E_\perp/E_\parallel$ (Podesta 2009), as a function of $\kappa^*$. The results of this analysis are displayed in Figure 2, where individual intervals are plotted as scatter points and binned based on their $\sigma_c$ value. The median curve for each bin is shown, and the color of each curve is keyed to $\sigma_c$. The median curve (black solid line) in Figure 2 is consistent with previous findings at larger heliocentric distances. Specifically, the curve exhibits a region of near isotropy for $kd_i \lesssim 10^{-3}$, which roughly corresponds to the rollover to the $f^{-1}$ range of the magnetic spectrum (see Figure 1). At smaller scales, the anisotropy becomes more noticeable and shows a power-law scaling that closely resembles the $1/3$ value suggested by the CB conjecture. Therefore, a line with a scaling exponent of $1/3$ was included in the figure as a point of reference. This $\kappa^* 1/3$ scaling is observed within the range of $4 \times 10^{-2} - 3 \times 10^{-1} [d_i^{-1}]$, which corresponds to region $R^2$ in Figure 1. Additionally, while the anisotropy increases at smaller scales until $\kappa d_i \approx 4 \times 10^{-1}$, there is a sudden but noticeable local minimum at around $\kappa d_i \approx 0.7$ followed by a local maximum at $\kappa d_i \approx 1.7$. Both the trough and peak are consistently observed across all intervals considered in this study. The local minimum may be caused by the bump observed in $E_\parallel$ at $\kappa d_i \approx 0.06$, which coincides with the beginning of the transition region in $E_\perp$ (see Figure 1). This bump may suggest a local enhancement of energy that could be due to ion kinetic instabilities (Wicks et al. 2010). For a more comprehensive discussion of the double-peak structure in Figure 2(a), see Podesta (2009). The results of this study differ from those of Podesta (2009) in that we observe an increase in anisotropy at smaller scales $\kappa d_i > 2$. As shown in Figure 7 of Podesta (2009),
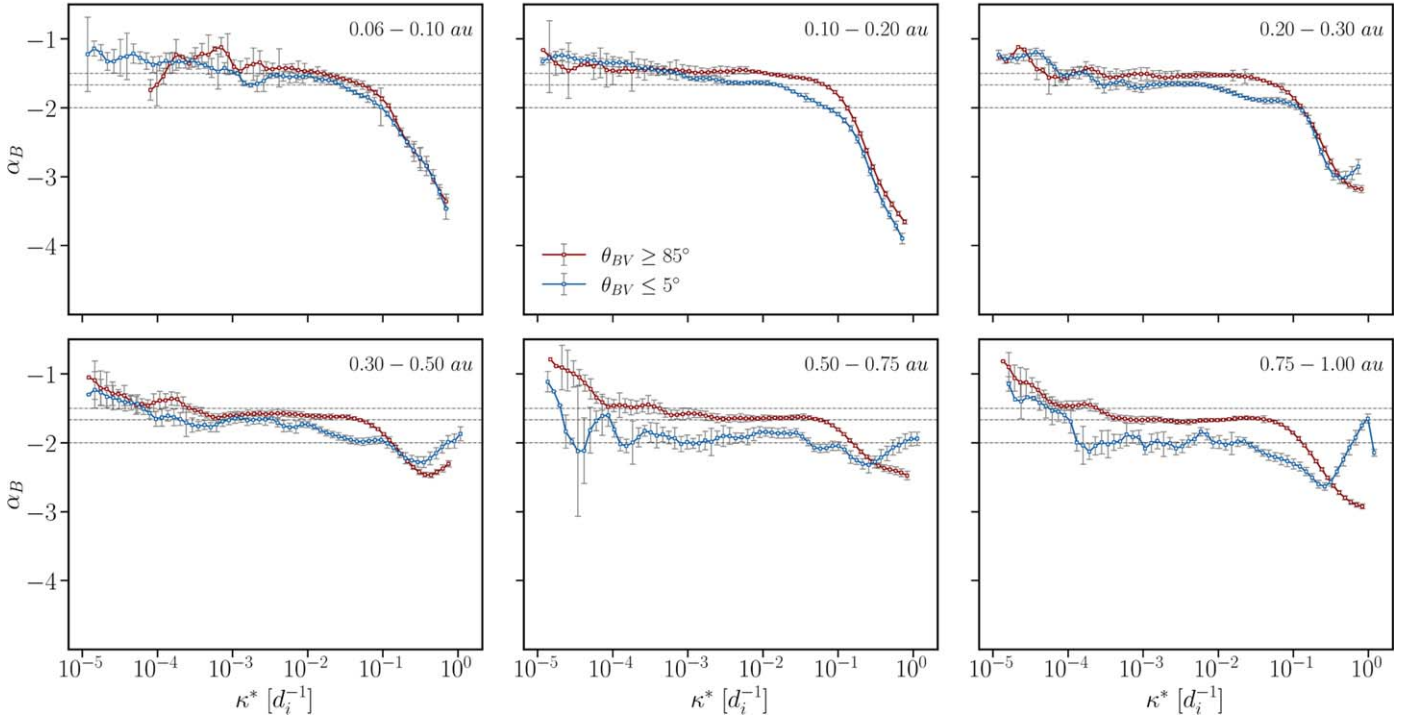
**Figure 3.** The local spectral index ($\alpha_B(\kappa^*)$) for fluctuations with $\theta_{BV} \leqslant 5°$ (blue), and $\theta_{BV} \geqslant 85°$ (red) at different heliocentric distances for slow streams, $V_{sw} \leqslant 400$ km s$^{-1}$. The local spectral index was calculated for all selected intervals, and each curve corresponds to the mean of all intervals that fall inside the bins indicated in the legend. We focus on MHD scales, $\kappa d_i \leqslant 3 \times 10^{-1}$, because instrumental noise flattens the PSD with increasing distance, as discussed in Section 4.1.

a rapid decrease in the power ratio is observed beyond the local kinetic scale maximum of approximately 1 Hz, which is attributed to the dissipation of kinetic AWs. However, as the spacecraft moves farther away from the Sun, the amplitude of the fluctuations at kinetic scales is close to the noise floor of the magnetometer. This can lead to an artificial steepening of the PSD caused by instrumental noise (Woodham 2019). The effect is particularly significant for $\alpha_B(\kappa^*)$ parallel, as most of the power in the solar wind is associated with perpendicular fluctuations. As a result, the parallel PSD systematically obtains lower values at MHD and kinetic scales and is therefore more likely to be affected by instrumental noise. On the other hand, the perpendicular PSD can remain intact. This can cause the parallel PSD to flatten out and the power ratio to decrease with decreasing scale. Considering that (1) the aforementioned paper uses magnetic field data from the STEREO mission (Acuña et al. 2008) at Earth orbit, where the turbulence amplitude is lower compared to that observed by PSP's E1, and (2) the SCaM data product merges FGM and search-coil magnetometer measurements, allowing for magnetic field observations up to 1 MHz with an optimal signal-to-noise ratio, we attribute the discrepancy to instrumental noise that may have affected the parallel PSD in Figure 7 of Podesta (2009).

### 4.2. Radial Evolution of Anisotropic Turbulence

#### 4.2.1. Spectral Index Anisotropy

In the following, we investigate the evolution of spectral index anisotropy with heliocentric distance. For this analysis we consider intervals sampled by the PSP and SO at distances between 0.06 and 1 au (see Section 3.2). Previous research has shown that the dominant orientation of fluctuation wavevectors in fast solar wind streams tends to be quasi-parallel to the local

magnetic field, while in slow solar wind streams the dominant orientation is quasi-perpendicular (Dasso et al. 2005). In order to examine the distinct features of each type of stream and their potential impact on the development of anisotropy in the solar wind, a comprehensive visual analysis was undertaken to categorize the streams into two distinct groups: slow streams characterized by $V_{sw} \leqslant 400$ km s$^{-1}$ and fast streams with $V_{sw} \geqslant 400$ km s$^{-1}$. A comprehensive record of the chosen intervals can be accessed in MHDTurbPy.

We shall begin by examining the evolution of slow streams, which compose the majority of the samples collected from PSP and SO. To determine the local spectral index for each interval, we perform calculations in the direction parallel ($\theta_{BV} \leqslant 5°$) and perpendicular ($\theta_{BV} \geqslant 85°$) to the locally dominant magnetic field, utilizing a sliding window of size $w = 10$, following the methodology outlined in Section 4.1.

We then partitioned our intervals into six heliocentric bins and calculated the mean local spectral index for those intervals that fell within each bin. It should be noted that despite the spectra and local spectral indices being calculated at identical frequencies based on the interval duration and sampling frequency, the normalization process results in an irregular shift along the vertical axis. Consequently, we divided the complete range of $\kappa^*$ into 100 bins and computed the mean for all $\alpha_B(\kappa^*)$ values that fell within each bin, as described in Němeček et al. (2021). It is worth noting that the size of the interval under consideration does not have a significant impact on the outcomes. This is true as long as a sizable statistical sample of fluctuations is taken into account at a given scale, in order to ensure the validity of the statistical analysis and produce accurate spectra (Dudok de Wit et al. 2013). Any intervals that exhibited noisy or otherwise unreliable spectra were excluded from subsequent analyses. However, it is
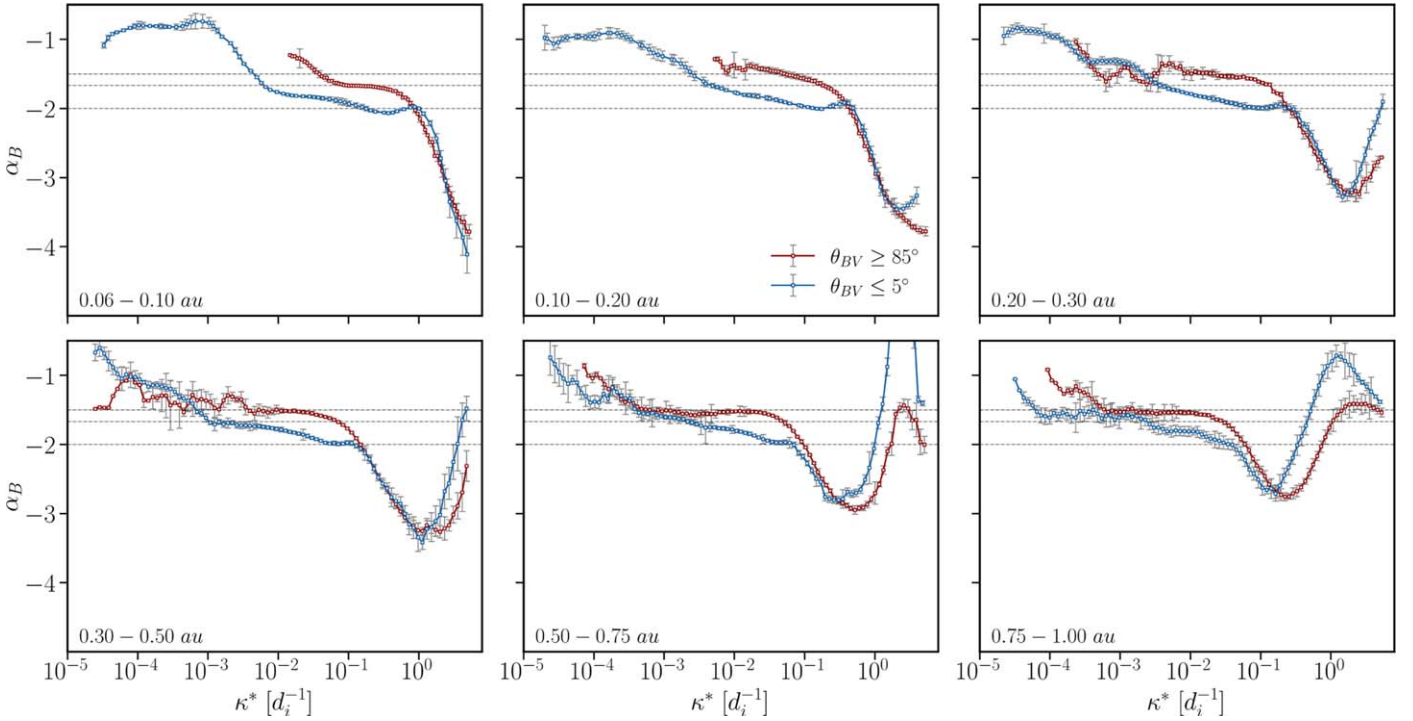
**Figure 4.** The local spectral index ($\alpha_B(\kappa^*)$) for fluctuations with $\theta_{BV} \leqslant 5°$ (blue) and $\theta_{BV} \geqslant 85°$ (red) at different heliocentric distances for fast streams, $V_{sw} \geqslant 400$ km s$^{-1}$. The local spectral index was obtained for all selected intervals, and each curve corresponds to the mean of all the intervals that fall inside the bins indicated in the legend.

important to note that such intervals made up only an inconsequential proportion of the overall data set.

The radial size of each bin is shown in the legend of Figure 3. The slow wind local spectral indices, as a function of heliocentric distance, are shown in blue for perpendicular fluctuations and in red for parallel fluctuations, along with error bars indicating the standard error of the mean. The standard error is given by $\sigma_i/\sqrt{N}$, where $\sigma_i$ is the standard deviation and $N$ is the number of samples inside the bin, as described in Gurland & Tripathi (1971). We focus our attention on MHD scales, $\kappa d_i \leqslant 3 \times 10^{-1}$, here simply because instrumental noise artificially steepens the PSD with increasing distance, as discussed in Section 4.1.

It is evident from Figure 3 that the spectral index anisotropy of slow wind turbulence diminishes closer to the Sun. Within 0.1 au, both parallel and perpendicular spectra are characterized by a poorly developed inertial range, viz., the range of scales over which the spectral index is constant is limited to $3 \times 10^{-3} \lesssim \kappa d_i \lesssim 2 \times 10^{-2}$, with a scaling exponent $-1.47 \pm 0.04$ and $-1.55 \pm 0.05$ for perpendicular and parallel fluctuations, respectively. At distances 0.1–0.2 au, two subranges ($R^1$ and $R^2$) emerge within the inertial range. The transition occurs at $\kappa d_i \approx 6 \times 10^{-2}$, and the scaling exponents in these ranges are similar to those shown in Figure 1. However, the steepened region $R^2$ is not as well defined in this case. Considering that the PSP was at a distance of 0.17 au during E1, we attribute this discrepancy to the fact that $R^2$ actually appears closer to 0.2 au. By shifting the left boundary of the bin toward 0.2 au, we confirmed this expectation, as the steepened region displayed a parallel power-law scaling of $-2$ when the left boundary was shifted to approximately 0.15 au.

In $R^1$ both parallel and perpendicular spectra dynamically evolve with increasing distance and steepen toward $-5/3$, which in the case of the parallel spectrum occurs within 0.1 au. The

steepening occurs in a scale-dependent fashion, which results in $R^2$ extending to larger scales with distance. As a result, for distances exceeding 0.5 au, $R^1$ practically vanishes, and the power spectra are characterized by a power-law exponent that changes from $-5/3$ in the direction perpendicular to $-2$ in the direction parallel to the locally dominant mean field, in good agreement with the predictions of CB theory. It should be noted that the analysis was iterated over bins of width 10°, yielding consistent outcomes. Notably, the obtained PSDs for $\theta_{BV} \geqslant 80°$ or $\theta_{BV} \geqslant 85°$ exhibited indistinguishable scaling behavior across all distances. Conversely, a comparison of the PSDs obtained for $\theta_{BV} \leqslant 10°$ and $\theta_{BV} \geqslant 5°$ revealed marginally steeper scaling behavior in the latter case for the inertial range. Specifically, in the instance of slow solar wind intervals, when distances exceeded 0.5 au, a consistent $-2$ scaling was observed for $\theta_{BV} \geqslant 5°$, whereas for $\theta_{BV} \geqslant 10°$ the scaling behavior obtained was closer to $-1.89$.

We next examined the evolution of fast streams ($V_{sw} \geqslant 400$ km s$^{-1}$). It is important to consider that as the solar wind expands in the heliosphere, the local mean magnetic field vectors become increasingly oriented at larger angles relative to the radial direction. This radial trend causes sampling at 0.06 au to be more quasi-longitudinal and sampling at 1.0 au to be more quasi-perpendicular. As parallel fluctuations decrease with increasing distance, our ability to accurately estimate the low-frequency part of the parallel power spectrum is reduced. This effect makes the determination of the anisotropic scaling laws for high-speed streams in the ecliptic plane challenging, as there is insufficient data to make accurate measurements at low frequencies. While using longer records could resolve this issue, the limited lifetime of the streams restricts the length of the record. In an effort to address this issue, we imposed a minimum interval length that would allow for a large enough interval size but still enable us to gather a sufficient number of intervals for
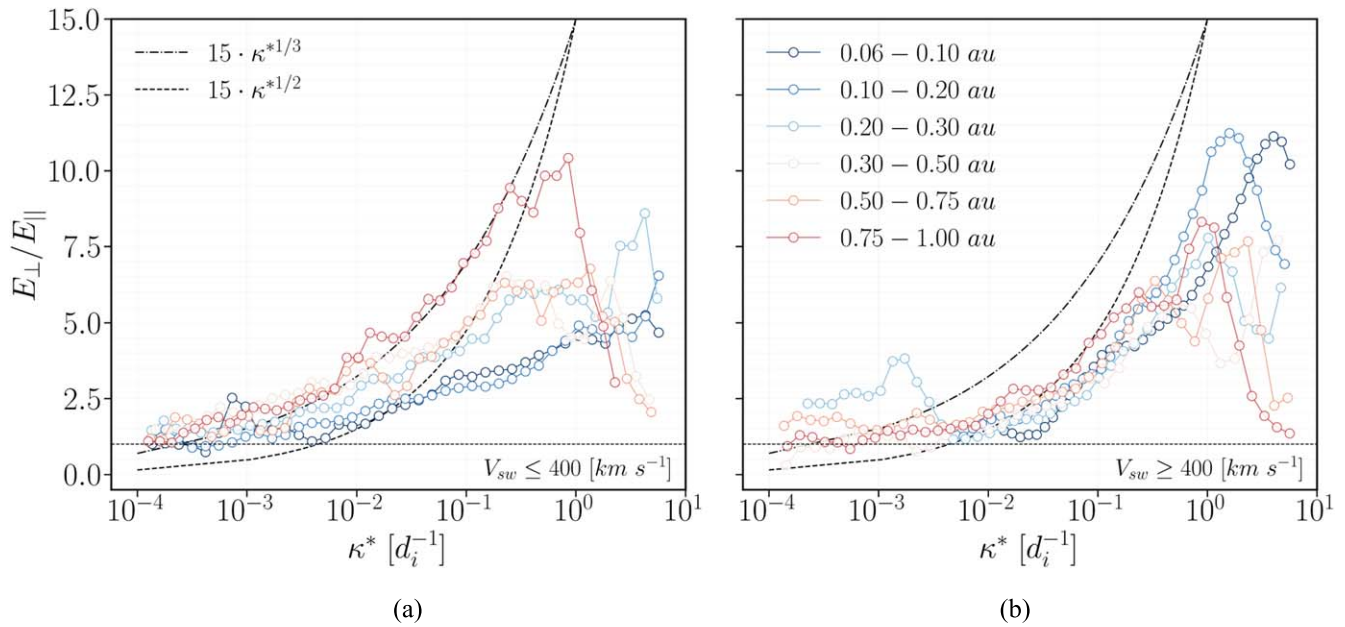
(a)                                        (b)

**Figure 5.** The radial evolution of the power anisotropy, represented by the ratio $E_\perp/E_\parallel$, is depicted as a function of heliocentric distance for slow ($V_{sw} \leqslant 400$ km s$^{-1}$) and fast ($V_{sw} \geqslant 400$ km s$^{-1}$) streams. Six heliocentric-radius bins were utilized, and each curve represents the median of $E_\perp/E_\parallel$ from all intervals that fall within each bin. The dashed ($y = 15 \cdot \kappa^* 1/2$) and dashed–dotted ($y = 15 \cdot \kappa^* 1/3$) lines were added as reference points, indicating consistency with a "dynamically aligned" and "critically balanced" cascade, respectively.

our statistical study. Specifically, for heliographic distances exceeding 0.3 and 0.5 au, we set the minimum interval size to 12 and 20 hr, respectively. This resulted in a total of 274 intervals sampled across the inner heliosphere. The results of this analysis are presented in Figure 4. It is readily seen that the differences between fast and slow intervals are significant. When examining the lower frequencies, we observe that within 0.2 au the energy injection range of the PSD is dominated by parallel fluctuations. In particular, a remarkably extended and relatively shallow range with $\alpha_B \approx -0.8$ is observed within 0.1 au, which steepens toward $-1$ with distance. This is particularly noteworthy, as previous research has shown that AWs can parametrically decay into slow magnetosonic waves and counterpropagating AWs (Galeev & Oraevskii 1963; Tenerani et al. 2017; Malara et al. 2022). This process may lead to the development of a $k_\parallel^{-1}$ spectrum for outward-propagating AWs by the time they reach a heliocentric distance of 0.3 au in the fast solar wind (Chandran 2018). For a more comprehensive investigation of the radial evolution of the lower-frequency part of the spectrum, see Huang et al. (2023). Due to the issues with interval size that were discussed earlier, we do not attempt to interpret the evolution of the lower-frequency part of the spectrum beyond 0.3 au.

Focusing on MHD scales, we notice that the perpendicular PSD only extends up to $\kappa d_i \approx 10^{-2}$. This implies that fast streams in proximity to the Sun exhibit a nearly radial magnetic field at low frequencies. Interestingly, within 0.1 au, the scaling of the perpendicular spectrum is consistent with $-5/3$, but at larger distances a scaling that is roughly consistent with $-3/2$, fluctuating between $-1.49$ and $-1.55$, is observed. This suggests that the MHD range spectral index of the perpendicular spectrum for fast streams may not evolve in a consistent manner with increasing distance in the inner heliosphere. It is worth noting, however, that within 0.1 au only four intervals with $V_{sw} \geqslant 400$ km s$^{-1}$ were sampled by PSP. More data from fast streams near the Sun are needed to statistically confirm these

findings. For parallel fluctuations, the inertial range scaling remains remarkably similar across all heliographic bins, with the spectral index progressively steepening toward smaller scales from $-5/3$ toward $-2$, where a narrow range of scales over which the local spectral index obtains a constant value appears. In contrast to slow wind streams, the high-frequency point in fast wind streams does not remain anchored in a normalized wavenumber but gradually drifts toward larger scales with distance. This is an interesting finding that suggests that the evolution of the high-frequency point is different between fast and slow wind streams; this is discussed further in Section 5.

### 4.2.2. Power Anisotropy

In this section we examine the radial evolution of the power anisotropy, represented by the ratio $E_\perp/E_\parallel$, where $E_\perp$ and $E_\parallel$ are the PSDs for $\theta_{BV} \geqslant 85°$ and $\theta_{BV} \leqslant 5°$, respectively. To do this, we utilized the method described in Section 4.2.1 and calculated the mean of $E_\perp/E_\parallel$ in six heliocentric bins. The results of this analysis are presented in Figure 5(a) for slow streams and Figure 5(b) for fast streams. According to theories based on "dynamical alignment," the inertial range scaling index should be 1/2 when considering $E_\perp/E_\parallel$, while a slope of 1/3 is predicted by CB theories.

For slow wind streams, the power anisotropy becomes more significant with increasing distance, particularly at smaller scales (see Figure 5(a)). This suggests that the turbulence undergoes an anisotropic cascade, transporting the majority of its magnetic energy toward larger perpendicular wavenumbers. In contrast, fast streams show practically no significant radial trend, especially when taking into account the error bars (not shown here). As a result, even though the power anisotropy is more pronounced for fast winds closer to the Sun, at distances of around 1 au, the situation is reversed, and slow wind exhibits higher values of $E_\perp/E_\parallel$. In terms of anisotropic scaling, we observe that $E_\perp/E_\parallel$ evolves in a manner similar to what was

described in Section 4.2.1. Specifically, the scaling of $E_\perp/E_\parallel$ for slow wind streams does not fit the predictions of any of the existing anisotropic theories closer to the Sun, but with increasing distance, it evolves toward a scaling that is consistent with CB theories. The situation is more complex for fast streams. In particular, for the bin closest to the Sun, the scaling of $E_\perp/E_\parallel$ is closer to that predicted by CB theories ($\kappa^*1/3$), but for the rest of the bins, the scaling exponent fluctuates in the range between $1/2$ and $1/3$. Additionally, the double-peak structure discussed in Section 4.1 is also observed for most of the curves in this analysis, especially in fast wind intervals. In contrast to the data presented in Section 4.1, at smaller scales the utilization of FGM data leads to a significant impact of instrumental noise on the resulting curves, ultimately causing a marked decrease in the power ratio.

## 5. Discussion

Wavelet analysis of solar wind data obtained at heliocentric distances greater than 0.3 au has shown strong agreement between the anisotropic characteristics of magnetic turbulence and the predictions of the CB conjecture (Horbury et al. 2008; Wicks et al. 2010). However, Podesta (2009) cautioned that it would be premature to draw conclusions about the agreement of the scaling in the fast solar wind with any particular theory owing to the large uncertainties of the scaling at the largest scales. It is worth noting that these studies focused on either high-speed streams or prolonged periods of both high-speed and slow streams (Horbury et al. 2008; Wicks et al. 2010, 2013; He et al. 2013). When extended intervals are considered, the PSD behavior will be practically determined by the fast subintervals since high-speed streams exhibit higher-amplitude magnetic fluctuations. Recent PSP measurements below 0.3 au have provided an unprecedented opportunity to study the nature of the solar wind in the vicinity of the solar wind sources. Bandyopadhyay & McComas (2021) and Adhikari et al. (2022) have recently shown that large-scale fluctuations in the near-Sun solar wind are dominated by wavevectors quasi-parallel to the local magnetic field. Zhao et al. (2022) also studied the radial dependence of this ratio by grouping the available data sets into two catalogs according to the radial distance and found that the ratio between parallel and perpendicular fluctuations observed by PSP is about 50%: 50%.

Inertial range spectral anisotropy has been investigated by Huang et al. (2022) and Wu et al. (2022), who used slow solar wind data from E1 of PSP to show that the spectral indices are close to $-5/3$ and $-3/2$ in the parallel and perpendicular direction, respectively. Wu et al. (2022) further conducted a comparative analysis of the anisotropic spectral properties of the slow wind stream observed by PSP during E1 and a fast wind stream with a solar wind speed $V_{sw} \approx 770$ km s$^{-1}$, which was sampled by Ulysses at 1.48 au. Their analysis led to the conclusion that the dynamical evolution of the inertial range scaling can be attributed to the existence of two subranges in the inertial range. Specifically, the subrange closer to the kinetic scales, $30d_i-300d_i$, exhibits a radial steepening, while the subrange at larger scales remained unchanged. As demonstrated by Wu et al. (2022), the transition between the two ranges in question does not exhibit radial evolution, but rather remains constant in terms of $\kappa d_i$. Nevertheless, the reliability of this finding is uncertain given the contrasting radial evolutions of fast and slow streams based on turbulence signatures, as reported by Shi et al. (2021) and Sioulas et al. (2022a, 2022b).

There are several significant questions that remain unanswered regarding the anisotropy of magnetic turbulence in the solar wind and its evolution as it propagates into the heliosphere. First, it is unclear whether the anisotropy dynamically evolves with distance. Second, there is a need to investigate potential differences in spectral and power anisotropy between fast and slow streams, and if such differences exist, it is important to determine whether they evolve with distance. In the subsequent section, we endeavor to address these outstanding issues by comparing our findings with those of previous studies.

## 6. Comparison with Prior Investigations

### 6.1. Horbury et al. (2008) and Podesta (2009)

In our study, using data from PSP and SO, we estimated perpendicular inertial range spectral indices for the fast wind with values in the range of $[-1.49, -1.55]$. These values are slightly shallower than those reported in previous studies (Horbury et al. 2008; Podesta 2009; Wicks et al. 2010), which estimate values in the range of $[-1.55, -1.67]$. One possible reason for this discrepancy could be that the PSP and SO data were only collected in the ecliptic plane during the minimum and early rising phase of the solar cycle. It is known that solar wind conditions can vary significantly over the course of the solar cycle, and it is possible that these variations could affect the observed scalings of the perpendicular spectra. In addition, due to the phase of the solar cycle, only a limited number of extended fast wind streams were collected. For example, PSP only sampled four intervals with $V_{sw} \geqslant 400$ km s$^{-1}$ within 0.1 au. This limitation may affect the statistical significance of the results and make it difficult to accurately measure the anisotropic scaling laws for these streams at lower frequencies. As a result, it may be premature to draw firm conclusions about the agreement of the scaling in the fast solar wind sampled in the ecliptic plane by PSP and SO with any particular theory of anisotropic MHD turbulence.

### 6.2. Wicks et al. (2010)

Our results indicate that, when analyzing slow wind streams, normalizing the PSD with $d_i$ allows us to fix the high-frequency break point, $f_b$, in normalized wavenumber space, as previously reported in Sioulas et al. (2022a). However, for fast solar wind streams, $f_b$ tends to shift toward larger $\kappa d_i$ as the distance increases. This phenomenon can be attributed to the fact that fast solar wind streams are characterized by higher proton temperatures ($T_p$; Maksimovic et al. 2020; Shi et al. 2021, 2023), which lead to higher plasma pressure and, consequently, higher plasma $\beta$ values. The plasma $\beta$ is defined as the ratio of thermal to magnetic pressure, $\beta \equiv n_p K_B T_p/(B^2/2\mu_0)$, and it is comparatively higher in fast streams than in slow ones. It should be noted that the $V_{sw} - \beta$ correlation was verified, although it is not presented in this report. Chen et al. (2014) and Vech et al. (2018) have shown that the $f_b$ of the magnetic PSD between inertial and kinetic scales correlates better with $d_i$ when the intervals are characterized by $\beta < 1$ values, while high $\beta$ intervals are characterized by a small-scale break at the thermal ion gyroradius ($\rho_i$). In line with this, our analysis confirms the findings of Wicks et al. (2010), who used five fast solar wind streams with $\beta > 1$ between 1.5 and 2.8 au and found that the small-scale end of the inertial range seems to naturally scale with the ion gyroradius when normalized with $\rho_i$. Given that $\rho_i$

grows radially as $\propto R^{1.48\pm0.02}$ (Sioulas et al. 2022a), we expect that $f_b$ will display a similar radial trend for fast solar wind streams.

### 6.3. Wu et al. (2022)

The use of high-resolution data from E1 of PSP allowed us to confirm the existence of two subranges (Telloni 2022; Wu et al. 2022) within the inertial range. The transition occurs at $\kappa d_i \approx 6 \times 10^{-2}$ and signifies a shift from $-5/3$ to $-2$ scaling in the parallel spectra and from $-3/2$ to $-1.57$ scaling in the perpendicular spectra. The difference between the two ranges $(R^1, R^2)$ is most apparent in the parallel spectrum and could signify a transition from weak to strong turbulence (Sridhar & Goldreich 1994; Meyrand et al. 2016; Zank et al. 2020). It is important to note that the parallel spectral index we report here for $R^2_{\parallel}$, $\alpha_B \approx -2$, is steeper than the one reported by Wu et al. (2022). It is unlikely that the variations seen in the outcomes are due to the utilization of structure functions in the analysis carried out by Wu et al. (2022). This is because we used second-order structure functions to confirm the anisotropic scaling. Nonetheless, it is feasible that the differences could be linked to the usage of better-quality SCaM data in our research. In particular, Wu et al.'s parallel structure function in Figure 4(b) seems to become steeper at shorter timescales, but the limited cadence of around 1 Hz might prevent the clear detection of such scaling.

Moreover, it has been observed that there exist noteworthy differences between fast and slow streams in terms of their anisotropic properties and dynamic evolution. Besides the distinctions noted in the evolution of the inertial range scaling, the high-frequency break point displays a more rapid shift toward lower frequencies in the analysis of fast wind streams. These findings are at odds with the assertions put forth by Wu et al. (2022) and emphasize the necessity of analyzing wind streams of comparable speeds for making meaningful comparisons.

### 7. Conclusions and Summary

We used a merged PSP and SO data set to study the dynamic evolution of turbulence anisotropy in the inner heliosphere, with a focus on understanding the differences in anisotropy observed between fast and slow wind streams

The main findings of our study can be summarized as follows.

For slow wind streams, $V_{\rm sw} \leqslant 400\,{\rm km\,s^{-1}}$, we find the following:

1. Within 0.1 au, the spectral index anisotropy of the inertial range vanishes, and the inertial range is confined to $3 \times 10^{-3} \lesssim \kappa d_i \lesssim 2 \times 10^{-2}$. The scaling exponents are $-1.47 \pm 0.04$ and $-1.55 \pm 0.05$ for perpendicular and parallel fluctuations, respectively. The power anisotropy $(E_\perp/E_\parallel)$ is weaker compared to previous studies at 1 au, and its inertial range scaling does not fit any predictions of anisotropic theories of turbulence.
2. At $\approx 0.15$ au two inertial subranges $(R^1, R^2)$ emerge. The transition occurs at $\kappa d_i \approx 6 \times 10^{-2}$ and signifies a shift from $-5/3$ to $-2$ and from $-3/2$ to $\approx -1.6$ scaling in parallel and perpendicular spectra, respectively.
3. Beyond this point, the power anisotropy monotonically strengthens with distance, indicating an anisotropic turbulent cascade that transports most of its magnetic energy toward larger perpendicular wavenumbers. Additionally, region $R^2$ extends toward smaller wavenumbers, gradually "consuming" region $R^1$. This process results in a scale-dependent steepening of the inertial range.
4. At distances exceeding 0.5 au, region $R^1$ practically vanishes, and the power spectra are characterized by a power-law exponent that changes from $-5/3$ in the direction perpendicular to $-2$ in the direction parallel to the locally dominant mean field, in good agreement with the predictions of CB.
5. The rate at which the high-frequency break point $f_b$ of the magnetic power spectrum drifts to lower frequencies with distance scales naturally with the rate at which the ion inertial scale, $d_i$, grows with distance. In other words, the high-frequency point $f_b$ is observed to remain anchored in $\kappa d_i$.

For fast streams, $V_{\rm sw} \geqslant 400\,{\rm km\,s^{-1}}$, we find the following:

1. Closer to the Sun, the energy injection range, $\kappa d_i \leqslant 10^{-3}$, of the spectrum is dominated by parallel fluctuations. Within 0.1 au, this range exhibits a quite extended shallow region with a scaling index of $\approx -0.8$. This region appears to steepen toward $-1$ with increasing distance, providing evidence for the parametric decay instability as a generating mechanism for the $k_\parallel^{-1}$ spectrum in the fast solar wind (Chandran 2018).
2. In MHD scales, the scaling of both the parallel and perpendicular spectra does not exhibit a clear radial trend. Within 0.1 au, the scaling of the perpendicular spectrum is consistent with $-5/3$. Beyond 0.1 au, the perpendicular spectral index fluctuates between $-1.49$ and $-1.55$. For parallel fluctuations, the inertial range scaling remains remarkably similar across all heliographic bins. The spectral index progressively steepens toward smaller scales from $-5/3$ toward $-2$, where a narrow range of scales over which the local spectral index obtains a constant value is observed.
3. Power anisotropy for fast streams does not seem to display a clear trend with distance. In terms of inertial range scaling, we find that fast streams are more consistent with the Boldyrev (2006) model based on "dynamical alignment" than the Goldreich & Sridhar (1997) model based on CB, but the large uncertainties at lower frequencies make the statistical significance of this result questionable.
4. In agreement with Wicks et al. (2010), the high-frequency point $f_b$ is observed to remain anchored in $\kappa \rho_i$.

A deeper understanding of anisotropy could be gained by considering the effect of intermittency on turbulence (Oboukhov 1962), i.e., the concentration of fluctuation energy into smaller volumes of space at smaller scales. Recent research has demonstrated a connection between CB and dynamic alignment with intermittency (Chandran et al. 2015; Mallet & Schekochihin 2017). A more comprehensive analysis comparing the anisotropic scaling of higher-order moments to existing theories is in progress.

When analyzing turbulence in the inner heliosphere, where the Alfvén speed approaches and sometimes exceeds the solar wind speed, special care must be used in applying homogeneous turbulence theories and models to the observed characteristics. This is especially important for power anisotropies, as, in

addition to wavenumber couplings, the couplings to large-scale gradients in both the radial and transverse directions may be fundamental, with the solar corona, for example, acting to refract energy in fast-mode polarization into regions of low Alfvén speed or even providing some total reflection. These couplings could also affect spectral slopes in the parallel and perpendicular directions in the nascent solar wind (Velli et al. 1991).

In conclusion, it is important to recognize the potential limitations of the current analysis, including the limited number of extended fast wind streams sampled by PSP and SO. These limitations may affect the statistical significance of the results and make it difficult to accurately determine the anisotropic scaling laws for these streams at lower frequencies. Therefore, it is advisable to continue collecting more samples from PSP and SO, particularly those of longer duration, to confirm the statistical significance of the findings. In addition, a more robust statistical analysis with longer intervals of data from Ulysses and Helios will be conducted to accurately determine the scaling of the anisotropy and its dependence on the heliocentric distance, phase of the solar cycle, and heliographic latitude.

### ORCID iDs

Nikos Sioulas https://orcid.org/0000-0002-1128-9685
Marco Velli https://orcid.org/0000-0002-2381-3106
Zesen Huang (黄泽森) https://orcid.org/0000-0001-9570-5975
Chen Shi (时辰) https://orcid.org/0000-0002-2582-7085
Trevor A. Bowen https://orcid.org/0000-0002-4625-3332
B. D. G. Chandran https://orcid.org/0000-0003-4177-3328
Ioannis Liodis https://orcid.org/0000-0002-8921-3760
Nooshin Davis https://orcid.org/0000-0001-7222-3869
Stuart D. Bale https://orcid.org/0000-0002-1989-3596
T. S. Horbury https://orcid.org/0000-0002-7572-4690
Thierry Dudok de Wit https://orcid.org/0000-0002-4401-0943
Davin Larson https://orcid.org/0000-0001-5030-6030
Michael L. Stevens https://orcid.org/0000-0002-7728-0085
Justin Kasper https://orcid.org/0000-0002-7077-930X
Christopher J. Owen https://orcid.org/0000-0002-5982-4667
Anthony Case https://orcid.org/0000-0002-3520-4041
Marc Pulupa https://orcid.org/0000-0002-1573-7457
David M. Malaspina https://orcid.org/0000-0003-1191-1558
Roberto Livi https://orcid.org/0000-0002-0396-0547
Keith Goetz https://orcid.org/0000-0003-0420-3633
Peter R. Harvey https://orcid.org/0000-0002-6938-0166
Robert J. MacDowall https://orcid.org/0000-0003-3112-4201

### References

Acuña, M. H., Curtis, D., Scheifele, J. L., et al. 2008, SSRv, 136, 203
Adhikari, L., Zank, G. P., Zhao, L.-L., & Telloni, D. 2022, ApJ, 933, 56
Alberti, T., Benella, S., Consolini, G., Stumpo, M., & Benzi, R. 2022, ApJL, 940, L13
Alberti, T., Laurenza, M., Consolini, G., et al. 2020, ApJ, 902, 84
Bale, S. D., Badman, S. T., Bonnell, J. W., et al. 2019, Natur, 576, 237
Bale, S. D., Goetz, K., Harvey, P. R., et al. 2016, SSRv, 204, 49
Bandyopadhyay, R., & McComas, D. J. 2021, ApJ, 923, 193
Belcher, J. W., & Davis, L., Jr. 1971, JGR, 76, 3534
Beresnyak, A., & Lazarian, A. 2010, ApJL, 722, L110
Bieber, J. W., Wanner, W., & Matthaeus, W. H. 1996, JGR, 101, 2511
Biskamp, D. 2003, Magnetohydrodynamic Turbulence (Cambridge: Cambridge Univ. Press)
Boldyrev, S. 2006, PhRvL, 96, 115002
Borovsky, J. E., Denton, M. H., & Smith, C. W. 2019, JGRA, 124, 2406
Bowen, T. A., Bale, S. D., Bonnell, J. W., et al. 2020, JGRA, 125, e27813
Bruno, R., Carbone, V., Sorriso-Valvo, L., & Bavassano, B. 2003, JGRA, 108, 1130
Chandran, B. D. G. 2018, JPlPh, 84, 905840106
Chandran, B. D. G., & Perez, J. C. 2019, JPlPh, 85, 905850409
Chandran, B. D. G., Schekochihin, A. A., & Mallet, A. 2015, ApJ, 807, 39
Chen, C. H. K., Bale, S. D., Bonnell, J. W., et al. 2020, ApJS, 246, 53
Chen, C. H. K., Horbury, T. S., Schekochihin, A. A., et al. 2010, PhRvL, 104, 255002
Chen, C. H. K., Leung, L., Boldyrev, S., Maruca, B. A., & Bale, S. D. 2014, GeoRL, 41, 8081
Chen, C. H. K., Mallet, A., Yousef, T. A., Schekochihin, A. A., & Horbury, T. S. 2011, MNRAS, 415, 3219
Chhiber, R. 2022, ApJ, 939, 33
Cho, J., & Vishniac, E. T. 2000, ApJ, 539, 273
Cuesta, M. E., Chhiber, R., Roy, S., et al. 2022, ApJL, 932, L11
Dasso, S., Milano, L. J., Matthaeus, W. H., & Smith, C. W. 2005, ApJL, 635, L181
Davies, L., & Gather, U. 1993, J. Am. Stat. Assoc., 88, 782
Dong, C., Wang, L., Huang, Y.-M., et al. 2022, SciA, 8, eabn7627
Duan, D., He, J., Bowen, T. A., et al. 2021, ApJL, 915, L8
Dudok de Wit, T., Alexandrova, O., Furno, I., Sorriso-Valvo, L., & Zimbardo, G. 2013, SSRv, 178, 665
Elsasser, W. M. 1950, PhRv, 79, 183
Galeev, A. A., & Oraevskii, V. N. 1963, SPhD, 7, 988
Galtier, S., Nazarenko, S. V., Newell, A. C., & Pouquet, A. 2000, JPlPh, 63, 447
Gerick, F., Saur, J., & von Papen, M. 2017, ApJ, 843, 5
Goldreich, P., & Sridhar, S. 1995, ApJ, 438, 763
Goldreich, P., & Sridhar, S. 1997, ApJ, 485, 680
Gurland, J., & Tripathi, R. C. 1971, Am. Stat., 25, 30, http://www.jstor.org/stable/2682923
He, J., Tu, C., Marsch, E., Bourouaine, S., & Pei, Z. 2013, ApJ, 773, 72
Higdon, J. C. 1984, ApJ, 285, 109
Horbury, T. S., Forman, M., & Oughton, S. 2008, PhRvL, 101, 175005
Horbury, T. S., O'Brien, H., Carrasco Blazquez, I., et al. 2020, A&A, 642, A9
Horbury, T. S., Wicks, R. T., & Chen, C. H. K. 2012, SSRv, 172, 325
Huang, S. Y., Xu, S. B., Zhang, J., et al. 2022, ApJL, 929, L6
Huang, Z., Sioulas, N., Shi, C., et al. 2023, ApJL, 950, L8
Hunter, J. D. 2007, CSE, 9, 90
Iroshnikov, P. S. 1963, AZh, 40, 742
Kasper, J. C., Abiad, R., Austin, G., et al. 2016, SSRv, 204, 131
Klein, K. G., Perez, J. C., Verscharen, D., Mallet, A., & Chandran, B. D. G. 2015, ApJL, 801, L18
Kraichnan, R. H. 1965, PhFl, 8, 1385
Lithwick, Y., Goldreich, P., & Sridhar, S. 2007, ApJ, 655, 269
Maksimovic, M., Bale, S. D., Berčič, L., et al. 2020, ApJS, 246, 62
Malara, F., Primavera, L., & Veltri, P. 2022, Univ, 8, 391
Mallet, A., & Schekochihin, A. A. 2017, MNRAS, 466, 3918
Maron, J., & Goldreich, P. 2001, ApJ, 554, 1175
Mason, J., Cattaneo, F., & Boldyrev, S. 2006, PhRvL, 97, 255002
Matteini, L., Horbury, T. S., Neugebauer, M., & Goldstein, B. E. 2014, GeoRL, 41, 259
Matthaeus, W. H., Goldstein, M. L., & Roberts, D. A. 1990, JGR, 95, 20673
McKinney, W. 2010, in Proceedings of the 9th Python in Science Conference, Vol. 445, ed. S. van der Walt & J. Millman (Austin, TX: SciPy), 51
Meyrand, R., Galtier, S., & Kiyani, K. H. 2016, PhRvL, 116, 105002
Moncuquet, M., Meyer-Vernet, N., Issautier, K., et al. 2020, ApJS, 246, 44
Montgomery, D., & Matthaeus, W. H. 1995, ApJ, 447, 706
Montgomery, D., & Turner, L. 1981, PhFl, 24, 825

Němeček, Z., Šafránková, J., Němec, F., et al. 2021, Atmos, 12, 1277

Ng, C. S., & Bhattacharjee, A. 1996, ApJ, 465, 845

Oboukhov, A. M. 1962, JFM, 13, 77

Osman, K. T., Matthaeus, W. H., Wan, M., & Rappazzo, A. F. 2012, PhRvL, 108, 261102

Oughton, S., Matthaeus, W. H., Wan, M., & Osman, K. T. 2015, RSPTA, 373, 20140152

Owen, C. J., Bruno, R., Livi, S., et al. 2020, A&A, 642, A16

Parker, E. N. 1979, Cosmical magnetic fields. Their origin and their activity (Oxford: Clarendon Press)

Perez, J. C., & Boldyrev, S. 2009, PhRvL, 102, 025003

Perez, J. C., Bourouaine, S., Chen, C. H. K., & Raouafi, N. E. 2021, A&A, 650, A22

Pi, G., PitÅa, A., Němeček, Z., et al. 2020, SoPh, 295, 84

Pine, Z. B., Smith, C. W., Hollick, S. J., et al. 2020, ApJ, 900, 93

Podesta, J. J. 2009, ApJ, 698, 986

Schekochihin, A. A. 2022, JPlPh, 88, 155880501

Schekochihin, A. A., Cowley, S. C., Dorland, W., et al. 2009, ApJS, 182, 310

Shebalin, J. V., Matthaeus, W. H., & Montgomery, D. 1983, JPlPh, 29, 525

Shi, C., Velli, M., Lionello, R., et al. 2023, arXiv:2301.00852

Shi, C., Velli, M., Panasenco, O., et al. 2021, A&A, 650, A21

Sioulas, N., Huang, Z., Shi, C., et al. 2022a, arXiv:2209.02451

Sioulas, N., Huang, Z., Velli, M., et al. 2022b, ApJ, 934, 143

Sridhar, S., & Goldreich, P. 1994, ApJ, 432, 612

Taylor, G. I. 1938, RSPSA, 164, 476

Telloni, D. 2022, FrASS, 9, 917393

Telloni, D., Sorriso-Valvo, L., Woodham, L. D., et al. 2021, ApJL, 912, L21

Tenerani, A., Velli, M., & Hellinger, P. 2017, ApJ, 851, 99

Van Rossum, G., & Drake, F. L., Jr. 1995, Python reference manual (Centrum voor Wiskunde en Informatica Amsterdam)

Vasquez, B. J., Smith, C. W., Hamilton, K., MacBride, B. T., & Leamon, R. J. 2007, JGRA, 112, A07101

Vech, D., Mallet, A., Klein, K. G., & Kasper, J. C. 2018, ApJL, 855, L27

Velli, M. 1993, A&A, 270, 304

Velli, M., Grappin, R., & Mangeney, A. 1991, GApFD, 62, 101

Verdini, A., Grappin, R., Alexandrova, O., & Lion, S. 2018, ApJ, 853, 85

Virtanen, P., Gommers, R., Oliphant, T. E., et al. 2020, NatMe, 17, 261

Wang, T., He, J., Alexandrova, O., Dunlop, M., & Perrone, D. 2020, ApJ, 898, 91

Weygand, J. M., Matthaeus, W. H., Dasso, S., et al. 2009, JGRA, 114, A07213

Wicks, R. T., Horbury, T. S., Chen, C. H. K., & Schekochihin, A. A. 2010, MNRAS Lett., 407, L31

Wicks, R. T., Mallet, A., Horbury, T. S., et al. 2013, PhRvL, 110, 025003

Woodham, L. 2019, PhD thesis, Imperial College

Wu, H., He, J., Yang, L., et al. 2022, arXiv:2209.12409

Zank, G. P., Nakanotani, M., Zhao, L.-L., Adhikari, L., & Telloni, D. 2020, ApJ, 900, 115

Zank, G. P., Zhao, L. L., Adhikari, L., et al. 2022, ApJL, 926, L16

Zhao, L. L., Zank, G. P., Adhikari, L., & Nakanotani, M. 2022, ApJL, 924, L5

Zhao, L. L., Zank, G. P., Adhikari, L., et al. 2020, ApJ, 898, 113